Monthly Notices
of the
ROYAL ASTRONOMICAL SOCIETY

MNRAS **483,** 917–930 (2019)
Advance Access publication 2018 October 24

doi:10.1093/mnras/sty2875

Modelling the radio and X-ray emission from T-Tauri flares

C. O. G. Waterfall ,★ P. K. Browning,★ G. A. Fuller★ and M. Gordovskyy
Jodrell Bank Centre for Astrophysics, School of Physics and Astronomy, The University of Manchester, Manchester, M13 9PL, UK

Accepted 2018 October 21. Received 2018 October 11; in original form 2018 June 12

ABSTRACT

T-Tauri stars are known for their high levels of magnetic activity and variability. Both classical and weak-line T-Tauri stars are overluminous in the radio compared with the well-established Güdel–Benz relation between radio and X-ray luminosity for solar and main sequence stellar flares. We show that there is little difference in the observational properties of classical T-Tauri stars and weak-line T-Tauri stars. We then model a typical T-Tauri – circumstellar disc system magnetosphere to predict the radio emission from flares associated with the circumstellar disc and accretion events. We assume that energetic electrons are generated in a large-scale magnetic flux tube due to a reconnection event with the accretion disc field at $4\,R_\odot$. Our standard model, with a dipolar magnetic field with a strength of 2 kG at the stellar surface and non-thermal and thermal densities of 2.5×10^{11} cm^{-3} and 5.0×10^{11} cm^{-3} respectively, produces both X-ray and radio emission consistent with observations ($\log L_X = 30.5$, $\log L_R = 16.3$). Varying the model parameters, we can reproduce the observed range of radio and X-ray emission. The peak radio luminosity and the frequency of this peak (which occurs at >10 GHz and possibly beyond 100 GHz for some sets of parameters) depend on the fraction of non-thermal particles and may be used as a diagnostic of this quantity. The surface field strength was varied from 0.5 to 7 kG, with the peak flux increasing by over three orders of magnitude. The models provide a framework for constraining the properties of these sources and to guide and interpret future observations.

Key words: accretion, accretion discs – magnetic reconnection – stars: flare – stars: variables: T Tauri, Herbig Ae/Be – radio continuum: stars.

1 INTRODUCTION

T-Tauri stars (TTSs) are low-mass ($<2\,M_\odot$) young stellar objects (YSOs). They are known for their high variability and magnetic activity which is frequently explained by flaring events or magnetospheric accretion bursts. These YSO flaring events are associated with magnetic reconnection in large loops that connect the star and circumstellar disc (Giardino et al. 2007; Orlando et al. 2011; López-Santiago et al. 2016). These loops have also been associated with magnetospheric accretion bursts (Alencar et al. 2012; Stauffer et al. 2014).

TTSs are subcategorized into two groups: the classical and weak-lined T-Tauri stars. The main characteristic that defines them is the presence or lack of a disc (Feigelson & Montmerle 1999; McKee & Ostriker 2007). The classical T-Tauri (CTT) stars possess large circumstellar discs from which they can accrete (Favata et al. 2005; Giardino et al. 2007; Getman et al. 2008; Hartmann, Herczeg & Calvet 2016; López-Santiago et al. 2016; Reale et al. 2018). On the other hand, weak-lined T-Tauris (WTTs) have far less significant discs and accretion but still show similarly large amounts of emission from their observed flaring events (Tsuboi et al. 1998; Giardino et al. 2006a; Uzawa et al. 2011).

Observations of flaring events on TTSs are frequently seen at both radio and X-ray wavelengths for both CTT and WTTs. Large X-ray and radio flares have been observed by Tsuboi et al. (1998), Gagné, Skinner & Daniel (2004), Giardino et al. (2006a), Grosso et al. (2007), Umemoto et al. (2009), and Uzawa et al. (2011) as well as numerous others. Grosso et al. (2007) specifically refer to the idea of magnetospheric accretion being the source of the flare in emission. The idea of an enhanced solar flare like event is also frequently mentioned. The radio emission is generally suggested to be due to gyrosynchrotron radiation from energetic electrons created by magnetic reconnection, but little detailed modelling has been undertaken to confirm this scenario.

Two scaling relations are relevant to this work and have both been applied to solar and main sequence stellar flares previously. The first is known as the Güdel–Benz relation (Güdel & Benz 1993). This is a correlation between thermal X-ray and non-thermal radio emission from coronae of magnetically active stars. The relation is

★ E-mail: charlotte.waterfall@postgrad.manchester.ac.uk (COGW); philippa.browning@manchester.ac.uk (PKB); g.fuller@manchester.ac.uk (GAF)

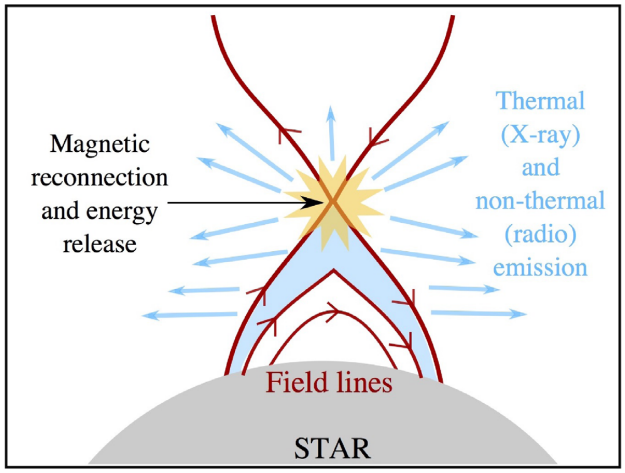

Figure 1. Diagram of a flaring event. Reconnection of oppositely directed magnetic field lines (red) occur at an X-point. The resulting gyrosynchrotron radiation and X-ray emission are shown in blue radiating outwards from the flux tube (shaded) and the reconnection site.

given by:

$$\frac{L_X}{L_R} \approx 10^{15.5} \quad (1)$$

where L_X and L_R are the X-ray and radio luminosity, respectively. The relation holds for the smallest microflares on the Sun up to the largest main sequence stellar flares.

The second relation concerns emission measures and temperatures, and shows that for a solar flare with a large emission measure there is a correspondingly large flare temperature. This second relation, developed by Shibata & Yokoyama (1999), leads to further relations regarding lengths of flaring loops and relevant surface magnetic field strengths. In this paper, both of these relations and their application to T-Tauri stars are explored. Both observational and simulation results of flares from T-Tauris are examined with respect to the Güdel–Benz relation.

The coronae of active stars produce significant amounts of X-ray and radio emission, as a result of magnetic reconnection. In a solar flare, the field loops are anchored into the solar surface and extend into the corona. This is illustrated in Fig. 1. Reconnection of oppositely directed field lines occurs at the X-point, resulting in the explosive release of energy, heating of plasma, and the acceleration of electrons along field lines (Benz 2008). The heated plasma produces thermal X-ray emission while the electrons gyrating along the field lines produce gyrosynchrotron radiation, i.e. non-thermal radio emission. This emission is ubiquitous to solar flares (Fletcher et al. 2011). The particles are either deposited down on to the footpoints incurring further heating and X-ray emission (a process known as chromospheric evaporation in a solar flare) or they are magnetically trapped and bounce back and forth, emitting further radiation.

The Sun and its flares are useful as a local analogue to T-Tauri flares. As T-Tauri stars are known to be highly variable with corresponding observed flaring activity (Feigelson & Montmerle 1999), we can use the solar flare model and the Güdel–Benz relation to understand more about these flares. Fig. 2 shows a basic schematic of a T-Tauri star and its magnetosphere. It is identifiable as a classical T-Tauri star by the inclusion of a circumstellar (or accretion) disc. While the magnetic loops involved in a solar flare may not range far from the surface, the flux tube in Fig. 2 is shown to extend

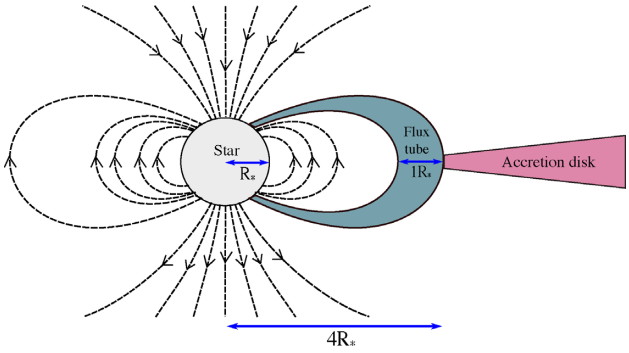

Figure 2. A schematic drawing to approximate scale of a classical T-Tauri star. The field lines of the magnetosphere are drawn in a dipolar configuration with a large flux tube shown to be interacting with the accretion disc. This interaction is expected to be the origin of a flaring-like event.

far into the magnetosphere and connect with the disc. Reconnection processes within the magnetosphere (and between the magnetic field loops and disc) are predicted to produce the thermal X-ray and non-thermal radio emission like in a solar flare. With this in mind, it might be expected that data from these objects would also agree with the Güdel–Benz relation.

While there is a substantial body of individual studies of variable radio emission in T-Tauri stars, there is little theoretical modelling to support interpretation of this work or to guide future observations. Our aim is to begin to address this. First (in Section 2), we collate observations from a range of published sources in order to investigate the extent to which flare-like events on T-Tauri stars conform with established scaling relations for solar flares and main sequence stellar flares, between radio and X-ray luminosities (Güdel & Benz 1993), and also between peak flare temperatures and emission measures (Shibata & Yokoyama 1999). We confirm that the T-Tauri stars deviate significantly from the Güdel–Benz relation. We then develop models which predict the radio and X-ray luminosities based on the physical parameters of the stellar atmosphere and the flaring region. The predicted distributions of radio and X-ray fluxes are in good agreement with the observations. A further goal of our models is to investigate the relationships between the physical parameters and the observable properties of the radio emission, in order to guide and interpret future observations.

It is likely that the physical processes in the T-Tauri flaring events are in many ways similar to solar flares, and therefore our understanding of the T-Tauri events can benefit from the large body of knowledge of solar flares. In particular, the energy release process in both cases is likely to be magnetic reconnection, which heats the plasma and also creates a significant population of non-thermal electrons; these gyrate around the magnetic field lines and emit gyrosynchrotron radiation in radio. However, the deviations from the scaling law suggest there are some underlying differences as well. We propose a scenario in which the flare results from magnetic reconnection between the stellar magnetic field and the accretion disc magnetic field. Thus, the location of the energy release, and hence the overall length-scale of the flaring region, is determined by the inner radius of the disc (see Fig. 2). Thus, the most obvious differences from solar flares is the much larger volume of the flaring region, as well as the stronger magnetic field. However, because the reconnection is driven by interactions with the disc (although not in a manner which is fully understood at present), and occurs in significantly different plasma conditions, the reconnection process

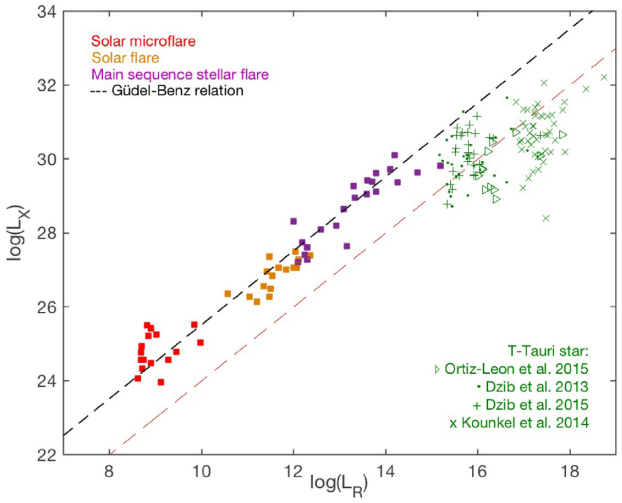

Figure 3. The peak X-ray and radio luminosities from various types of active stars are plotted. The Güdel–Benz relation (equation 1) and the modified Güdel–Benz relation (equation 2) are shown as black and red dashed lines, respectively. The colours correspond to different stellar flares as follows: red boxes are solar microflares (Benz & Güdel 2010), yellow are solar flares (Benz & Güdel 2010), purple are flares on other main sequence stars (Benz & Güdel (2010) and Güdel et al. (1993)), and the green symbols indicate observations of different T-Tauri stars (Dzib et al. (2013), Ortiz-León et al. (2015), Dzib et al. (2015) and Kounkel et al. (2014)). The majority of main sequence (including solar) flares agree well with the relation; however, there appears to be a divergence from the line of the T-Tauri flare data. The X-ray and radio bands used in these observations are given in Table 1.

may also differ from solar flares: thus, for example, the partitioning of released energy between thermal and non-thermal plasma might differ from the solar case.

We do not attempt to model the details of the magnetic interactions nor the energy release process, considering this only to be a source of plasma heating and of non-thermal electrons which fill a magnetic flux tube within the stellar magnetic field (the flaring region). Thus, we model a flux tube within the stellar atmosphere, which – similar to solar flares – has enhanced density and temperature with respect to the ambient corona, and also a population of non-thermal electrons. This model is detailed in Section 3.1.2. The various physical parameters for the flux tube and the ambient corona and magnetic field are chosen as far as possible to fit known properties of T-Tauri stars. The GX simulator (Nita et al. 2015) tool is then used to determine the X-ray and radio emission, and their dependencies on the underlying parameter space, such as temperature, magnetic field strength, and proportion of non-thermal electrons. Discussion of the initial results is given in Section 4 as well as results of varying the physical flux tube parameters.

2 SCALING RELATIONS OF OBSERVABLE QUANTITIES IN FLARES

2.1 Radio and X-ray luminosities: the Güdel–Benz relation

Observational data from T-Tauri stars has been collated from several published sources and is shown, along with the main sequence and solar data (previously plotted by Güdel & Benz 1993 and Benz & Güdel 2010), in Fig. 3. It is clear that the T-Tauri data do not agree with the Güdel–Benz relation to the same degree that the other solar and main sequence flare data do. The solar flare data (red and yellow) is gathered from Benz & Güdel (2010) and the main

Table 1. X-ray bands and radio frequencies of observational data from Figs 3 and 4. Radio references; [a]Ortiz-León et al. (2015), [b]Dzib et al. (2013), [c]Dzib et al. (2015), [d]Kounkel et al. (2014), [e]Güdel et al. (1993), [f]Güdel (1992), [g]Benz & Güdel (1994). X-ray references; [h]Kuhn et al. (2010), [i]Giardino et al. (2006b), [j]Pillitteri et al. (2010), [k]Imanishi et al. (2003), [l]Güdel et al. (2006), [m]Tsujimoto et al. (2002), [n]Skinner, Gagne & Belzer (2003), [o]Ramírez et al. (2004), [p]Getman et al. (2005).

Object	Radio frequency / GHz	X-ray band / keV
TTS (▷)	7.5 [a]	0.5–8.0 [h,i]
TTS (·)	7.5 [b]	0.3–10 [j,k]
TTS (+)	7.5 [c]	0.3–10 [l]
TTS (×)	7.5 [d]	0.3–10 [m,n,o,p]
Main sequence star	8.5 [e,f]	0.1–2.4, 0.2–4.0 [e,f]
Solar flare	8–9 [g]	0.1–2.4 [g]

sequence results (purple) are from Güdel et al. (1993) and Benz & Güdel (2010). The T-Tauri sources used in Fig. 3 are those defined in the literature to be flaring in either the radio or X-ray band. Sources were also included if they were noted as having high variability or a negative spectral index (possible indicators of a flaring event or the production of non-thermal emission). Sources that were explicitly labelled as quiescent were not included. The radio frequencies and X-ray bands used in all these observations are shown in Table 1 along with the original paper they are quoted from. All the sources have been observed at the same or similar radio frequency. The X-ray bands used are broader for the T-Tauri data than the solar and main sequence flares; however, they still cover approximately the same (lower energy) range.

These numerous observations of flaring activity from T-Tauri stars have identified the same thing: YSOs appear to be overluminous in the radio when compared with the solar and main sequence flares and the Güdel–Benz relation. There is no apparent connection between the deviation from the relation and the region that was observed. Dzib et al. (2015) suggested a modified Güdel–Benz relation for star forming regions of the form:

$$\frac{L_\times}{L_R} \approx 0.03 \cdot 10^{15.5}. \quad (2)$$

While this relation gives a better fit for the observational data in Fig. 3 (shown as the lower dashed line), it does not give any explanation as to why they do not fit with the original relation when other active stars do.

The discrepancy has been previously reported by Osten & Wolk (2009) (their observed sources are not shown on Fig. 3 although they show the same deviation from the relation). Their observation of the LkHα101 region in both X-ray and radio saw variability in flux at various time-scales but no correlation between the radio and X-ray emission. Their work remains one of few simultaneous radio and X-ray observations of the same region.

The solar flare model can be used as a basis for understanding these young stellar flares; however, it is clear that these events are born from more variable and active environments. Therefore, an enhanced flare model as well as other magnetospheric processes need to be considered. The large and more active magnetospheres of TTSs could lead to larger and more frequent reconnection events located further from the surface of the star. Interaction and accretion from the disc would lead to reconnection and flaring activity. Also, an extended magnetosphere is a prime candidate for a longer trapping time and further generation of gyrosynchrotron radiation without the intense heating of surrounding plasma associated with a reconnection event. An 'overproduction' of non-thermal radio emis-

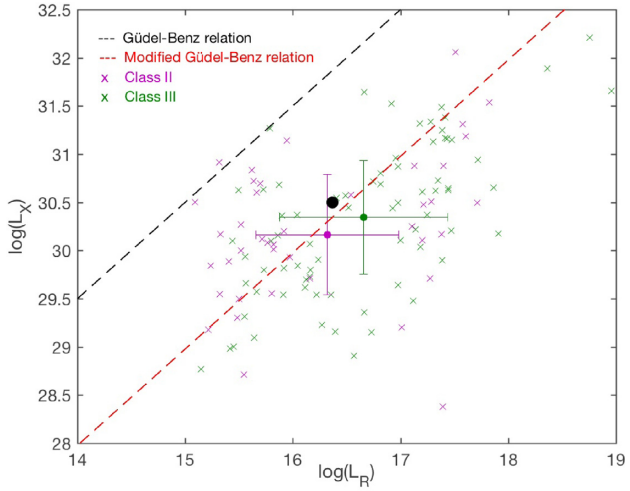

Figure 4. Closer view of Fig. 3 showing only the T-Tauri observations. The red dashed line is the modified Güdel–Benz relation given in equation (2). The black point is a result of a simulation of a T-Tauri flare and is discussed in Section 4. The observed T-Tauris are labelled according to their evolutionary stage. Purple crosses indicate a flare on a class II YSO, green represents a class III flare. The solid blue and green circles represent the mean value of the class II and class III sources, respectively, with their variances indicated by the error bars. The X-ray and radio bands used in these observations are given in Table 1.

sion compared with X-rays lends itself to the idea of large amounts of particle acceleration within the magnetospheres of these young stars.

A key property of the Güdel–Benz relation is that it involves non-thermal radio emission. If the radio observations of young stars are not confirmed to be purely non-thermal, this could lead to the over-luminosity seen in Fig. 3 (Forbrich, Osten & Wolk 2011). There are several criteria that can be used to determine non-thermal emission. If none of them are met, it can be difficult to prove the emission is non-thermal. This could lead to thermal emission being included in the results and therefore a more luminous result. However, the significant short-term variability of the sources (indicative of a magnetic reconnection event that produces gyrosynchrotron radiation) or the measured negative spectral index of their emission indicate that the emission is non-thermal in origin (Osten & Wolk 2009).

Whilst it is easy to explain the deviation seen in Fig. 3 as a result of the sources' heightened activity, it is worth noting the effect of Malmquist bias. The most luminous young stars observed here are from Orion at 414 pc (Kounkel et al. 2014) and are all located at the higher luminosity end in Fig. 3. This is the furthest region considered and suggests that only the most luminous events are picked up and there are likely numerous smaller events not registering. Overall, this is the case for every main sequence flare as well but they do correlate with the relation.

A closer view of the TTS's flare data from Fig. 3 for sources with a well-established class (class II or class III) is shown in Fig. 4. The deviation is clear with the modified Güdel–Benz relation (red dashed line) better matching sources. The radio observations shown in Fig. 4 were made at 7.5 GHz, corrected to the most recent distance estimates to the sources; however, all these sources were also observed at 4.5 GHz. These higher frequency observations show a very similar distribution to that in Fig. 4.

The lack of a circumstellar disc may lead to a decrease in emission due to reduced accretion. In principle, this can be assessed by examining the difference in Fig. 4 between classical and weak-lined T-Tauri stars, i.e. those with and without a disc. Overall, it is clear from Fig. 4 that a lack of disc does not lead to a decreased observed flux as the class III sources are distributed as evenly as the class II sources. Indeed, some of the most luminous flares are from class III stars.

Exploring the relationship between class II and class III sources further, a two-sample Kolmogorov–Smirnov test was carried out. First, the test is performed between the X-ray luminosity of the class II and class III objects. The test indicates that there is a probability of 16 per cent that two samples are drawn from the same population. In other words, there is no statistically significant evidence that the X-ray luminosity is different between these two groups of objects. Turning to the 7.5 GHz radio luminosity values, the probability that the two groups are from the same population is smaller, 7 per cent, but still formally insignificant. The same is true when the test is performed on the 4.5 GHz observations.

2.2 Emission measures and temperatures: the Shibata & Yokoyama relations

After considering the Güdel–Benz relation, we now discuss the physical parameters in a flare which could be causing the deviation from the relation. Examining these parameters through previously defined scaling relations (such as the one by Shibata & Yokoyama 1999) and recent observations will also enable us to derive the physical parameters needed to model a flaring scenario. The Shibata & Yokoyama (1999) relations in particular address the temperature, emission measure, and general size of the flaring region.

The emission measure (EM) from a certain flaring-like event is calculated using the equation:

$$EM = \int n_e^2 \mathrm{d}V \approx n_e^2 V, \tag{3}$$

where n_e is the density of the flaring plasma and V is the volume of the flaring loop ($V \approx L^3$ where L is the length of this region). Reconsidering the solar flare model, it is clear that with increased evaporation of chromospheric plasma from the heating of deposited particles comes an increase in the emission measure. An increased emission measure is therefore a good indicator of a flaring event occurring.

The temperature associated with the sudden heating of plasma in a reconnection event can be estimated along with the emission measures and plotted together as shown in Fig. 5. Shibata & Yokoyama (1999) suggested a universal correlation between emission measure and temperature for a wide range of flares including T-Tauri flares. The reasoning behind this claim is based on MHD numerical simulations of magnetic reconnection and the ensuing chromospheric evaporation. This relation suggested by Shibata & Yokoyama (1999) is given below in its full form along with a subsequent relation involving the flaring loop length,

$$EM \approx 10^{48} \left(\frac{B}{50\,\mathrm{G}}\right)^{-5} \left(\frac{n_0}{10^9\,\mathrm{cm}^{-3}}\right)^{\frac{3}{2}} \left(\frac{T}{10^7\,\mathrm{K}}\right)^{\frac{17}{2}} \mathrm{cm}^{-3} \tag{4}$$

$$EM \approx 10^{48} \left(\frac{L}{10^9\,\mathrm{cm}}\right)^{\frac{5}{3}} \left(\frac{n_0}{10^9\,\mathrm{cm}^{-3}}\right)^{\frac{2}{3}} \left(\frac{T}{10^7\,\mathrm{K}}\right)^{\frac{8}{3}} \mathrm{cm}^{-3}, \tag{5}$$

where B is the magnetic field strength, n_0 is the pre-flare density, and T is the flare peak temperature.

These relations, with constant n_0 and varying the magnetic field strength in equation (4) and loop length in equation (5), are shown in

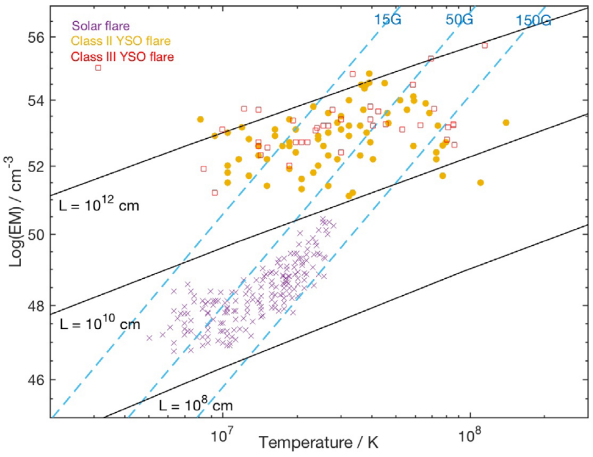

Figure 5. Flare peak temperatures and emission measures for flares on both the Sun (purple cross) and T-Tauris. Solar flare data are gathered from Feldman, Laming & Doschek (1995) and Shibata & Yokoyama (1999). The yellow circles represent class II (CTT) flares and red squares show class III (WTT) flares. TTS flare data are from Tsuboi et al. (1998), Imanishi, Koyama & Tsuboi (2002), Imanishi et al. (2003), Franciosini et al. (2006), Giardino et al. (2006a), Giardino et al. (2006b), Güdel et al. (2006), Grosso et al. (2007), Argiroffi et al. (2006), Getman et al. (2011), Schulz et al. (2015), and Tsuboi et al. (2016). The dashed blue lines represent the scaling relation in equation (4) (for constant n_0 and varying B values) and the solid black lines display the relation from equation (5) (for constant n_0 and varying L values).

the EM–T plot of Fig. 5. Also plotted are the data from several solar and TTS flares. Although the solar flare data does indeed appear to fit with the relation from equation (4) it does not extend in the same way to the T-Tauri data.

While the emission measures are a lot higher for the T-Tauri stars, the distribution is far flatter and more dispersed than for solar flares. For events with similar emission measure values, their flaring temperatures can vary greatly. Many of the T-Tauri events also suggest temperatures very similar to those of solar flares. It should be noted that the temperatures and emission measures for solar flare data are calculated using spectral line ratios (see Feldman et al. 1995). The X-ray bands used for the T-Tauri measurements are broad, therefore both of these methods should give accurate values and there should be no major inconsistencies in the measured temperatures.

Examining each event by categorizing it into which type of T-Tauri star it originates from does not reveal any differences between class II and III sources: both classical and weak-lined sources produce the same distribution in emission measures and temperatures. The individual region from which the sources are observed also show no bias. The method by which all these flares are measured is important. The young stellar data is collected from X-ray observations and the best-fit parameters are determined by spectral fitting. The spectral analysis of the X-ray data is predominately performed using XSPEC (a spectral fitting package) where the observed spectra is taken and compared to a parametrized model spectra. The model parameter values are manipulated until a best fit is found between the two spectra. The spectra are mostly fit with either a 1-temperature or 2-temperature model. As many of these fits used a 2-temperature model, only the higher recorded temperature (assumed to be the 'flaring' temperature) is plotted in Fig. 5. The same is true for emission measures. When the lower recorded temperature is used, both class II and III sources are shifted to the left of the plot. There is no change in the shape of the distribution of sources.

As the flaring loop length and emission measures are directly related, the lengths can also be investigated. It is known that T-Tauris possess large extended magnetospheres with assumedly large flaring loops also. Indeed for star–disc interactions to occur, the loops will need to reach to the inner edge of the circumstellar disc. These loop lengths are therefore expected to be far larger than those of solar flares. The associated loop length scaling relation is displayed as solid lines in Fig. 5 with the T-Tauris fitting into the largest loop length region. They extend up to around 10^{12}cm. This is over 10 times the solar radius which suggests large coronal loops. The inner radius of circumstellar discs of a star similar in size to the Sun is placed at around 5–10 R_* (Gregory et al. 2008; Johnstone et al. 2013). So, this scaling relation does suggest that these loops could reach and interact with the accretion disc as well. Numerical models and loop length calculations based on observations report similar loop lengths involved in star–disc interactions of around $10_{\odot}$ (Isobe et al. 2003; Giardino et al. 2007).

3 GYROSYNCHROTRON EMISSION MODEL

3.1 The model

3.1.1 GX simulator

The GX simulator was developed for modelling of microwave and X-ray emission from the Sun (Nita et al. 2015). It is based on fast calculation schemes for gyrosynchrotron (GS) emission developed by Fleishman & Kuznetsov (2010). The simulator models a 3D magnetic field, plasma, and energetic particle distribution in the solar atmosphere. Predefined magnetic fields are imported into the simulator in the desired configuration and flux tubes can then be populated with a distribution of thermal and non-thermal particles. These particles are added to the simple hydrostatic background plasma in a specified volume within a magnetic flux tube. Once all the parameters have been assigned, the model will generate spatially resolved X-ray and GS radio spectra.

The central source from which the magnetic field lines emerge from is modelled as the Sun, with the same (and unadjustable) mass and radius. The background coronal density, temperature, and scale height are all changeable as well as the location of the field lines on the surface. Once a flux tube is created, its general geometry as well as particle densities, temperature, electron distribution, and power law index are all modifiable.

A limitation of the GX simulator (due to the large loop lengths used) is the exclusion of foot points of the loop from the simulations (see Fig. 6). However, as we are modelling the emission from the loop top where the particles are injected (the thickest part, with the thickness kept the same in this region), it is not expected to drastically affect our results. We assume that the non-thermal and thermal volumes are the same simply because there is no capability to resolve this observationally and solar flare emitting volumes have been suggested to be of a similar order of magnitude (Warmuth & Mann 2013). However, that is not to say that because of the limitation stated above that we are assuming the non-thermal and thermal particles are only located at the loop apex; both emissions are found to extend to and occur at the foot points of a flaring loop in real life.

The GX simulator is predominantly used for work on the Sun but will be adapted here for use on a T-Tauri star. Those adaptations are

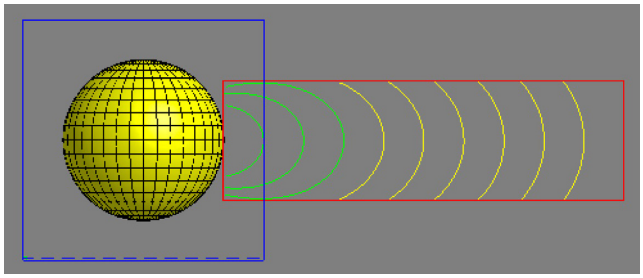

Figure 6. Image of the model from the GX simulator. The sphere, symbolizing the T-Tauri star, has the same mass and radius of the Sun. The lines shown in the box display the multipolar magnetic field configuration where the green and yellow represent closed and open lines, respectively. The furthest field line is converted into a flux tube and populated with non-thermal electrons in the model to simulate a reconnection event and the subsequent production of gyrosynchrotron radiation.

detailed in this section. The generation of radio spectra (and X-ray) from a modelled flaring-like event will be output and discussed in Section 4.

3.1.2 *The magnetic field model*

The GX simulator is used here to model the microwave radiation (including free–free from thermal electrons, gyrosynchrotron from thermal electrons, and gyrosynchrotron from non-thermal electrons) in a typical T-Tauri magnetosphere. Parameters such as flux tube densities and temperatures are all chosen to describe a young stellar environment but the mass and radius of the central object are maintained as $1\,M_\odot$ and $1\,R_\odot$. While a more typical radius of a YSO might be around $2\,R_\odot$, T-Tauri stars with radii around $1\,R_\odot$ have been reported (Johnstone et al. 2013).

The magnetic field configuration is imported into the simulator as a set of 3D arrays. The arrays describe the Cartesian components of the field strength at each point of the model data cube. The data cube is predefined in size and as we are interested in events that occur further out from the surface the data cube is set to extend to $4\,R_\odot$ ($=4\,R_*$).

One important factor of the T-Tauri model is the type of magnetic field configuration. Whereas a simple dipole field is easy to model, a multipolar field is more akin to the reported field of the stars. Hussain et al. (2009), Gregory & Donati (2011), and Long, Romanova & Lamb (2012) all use or suggest using a multipolar field in any model that deals with accretion. Therefore, a multipolar magnetic field of a dipole plus octupole is used with the dipole component having a greater dominance. Some YSOs have been suggested to have larger octupole components, e.g. V2247 Oph with a dipole and octupole component of 110 and 230 G, respectively (Johnstone et al. 2013). However, the 'typical' star AA Tau (a frequently observed and modelled class II YSO) has a field closer to that of a dipole with a non-negligible 0.5 kG octupole component (Donati et al. 2010).

The equations for magnetic field strength for this configuration are given in Cartesian coordinates as,

$$B_x = \frac{3}{2}B_{\rm dip}\left(\frac{R}{r}\right)^3\left(\frac{xz}{r^2}\right) + B_{\rm oct}\left(\frac{R}{r}\right)^5\left(\frac{35xz^3 - 15xzr^2}{8r^4}\right) \quad (6)$$

$$B_y = \frac{3}{2}B_{\rm dip}\left(\frac{R}{r}\right)^3\left(\frac{yz}{r^2}\right) + B_{\rm oct}\left(\frac{R}{r}\right)^5\left(\frac{35yz^3 - 15yzr^2}{8r^4}\right) \quad (7)$$

$$B_z = B_{\rm dip}\left(\frac{R}{r}\right)^3\left(\frac{3z^2 - r^2}{2r^2}\right) + B_{\rm oct}\left(\frac{R}{r}\right)^5 \times \left(\frac{3r^4 - 30z^2r^2 + 35z^4}{8r^4}\right), \quad (8)$$

where r is the distance from the centre of the star ($r = 0$), R is the stellar radius, and $B_{\rm dip}$ and $B_{\rm oct}$ are the surface dipolar and octupolar polar field strengths. These polar field strengths are related to the corresponding equatorial field strengths as (Gregory et al. (2010))

$$B_{\rm dip_{equator}} = \frac{1}{2}B_{\rm dip_{polar}} \quad (9)$$

for the dipolar component and,

$$B_{\rm oct_{equator}} = \frac{3}{8}B_{\rm oct_{polar}} \quad (10)$$

for the octupolar component.

Once imported into the GX simulator, the cube is populated with field lines as shown in Fig. 6. The field lines clearly appear to be dipolar, losing curvature with increasing radius from the star. The equatorial values of $B_{\rm dip}$ and $B_{\rm oct}$ chosen are discussed next in Section 3.2 but for reference the values that produce the field lines in Fig. 6 are 2000 G and 500 G. Where literature specifies the field strength, it is often quoted as an equatorial field strength. As the equations listed above use polar surface field strengths, the values used in the model are adapted appropriately. Henceforth, any mention of 'surface field strength' indicates an equatorial surface value.

The orientation of the field is important to consider when using this simulator. Conventionally the x, y, and z directions are represented on a sphere as being angled in the west (x) and north (z) direction with the y direction being given by the solar radius. However, for the GX simulator, the y coordinate acts in the northern direction and the z coordinate points radially out. Here, the length of the data cube stretches to $4\,R_\odot$ along the z axis.

To generate emission from this model, a field line is chosen at an appropriate 'interaction' radius (i.e. where the line could possibly meet with the circumstellar disc), modified into a flux tube, and populated with particles. The properties associated with this flux tube (temperature, densities, etc.) are drawn from observational evidence from young stellar flares and are discussed next.

3.2 Choosing suitable parameter values

First, we define a set of standard parameters for the various physical quantities relevant to the generation of radio and X-ray emission. These are determined, where possible, from published literature on T-Tauri stars, as well as on knowledge of solar flares. Subsequently, we consider effects of varying these parameters within reasonable ranges.

3.2.1 *Surface field strength*

As previously mentioned, the magnetic field is comprised of a dipole and octupole component. Surface magnetic field strengths are often quoted as being in the 1–2 kG range (Hartmann et al. 2016); however, they have been suggested to be as high as 6 kG in accretion spots (Donati et al. 2012; Johns-Krull et al. 2013). Some care must be taken in deriving values for our required parameters $B_{\rm dip}$ and $B_{\rm oct}$ from quoted 'surface field strengths', as these might be average values, or for a specific location.

Indeed Johns-Krull (2007) calculated that surface-averaged field strengths for individual classical T-Tauri stars are in the range 1220-2900 G. Dipolar specific values are sometimes quoted, as in Johnstone et al. (2013), to be around 1 kG for those TTSs with dimensions similar to our model. As it is thought the dipolar component is indeed the dominant factor in TTS's inner magnetospheres (Johns-Krull 2007), the reasonable assumption of a dipolar surface component of $B_{\mathrm{dip}_{\mathrm{equator}}} = 2$ kG is used in the model.

A value of 0.5 kG is used as the surface octupole component in this model, as suggested by Donati et al. (2010). Although this component had far less of an effect than the dipolar value, it is important to still include it to model a multipolar field. If a flux tube is being modelled at a distance closer to the surface the octupolar component would become more apparent. However, when the effects of a changing magnetic field strength are explored later on only the dipolar component is changed, as it makes a noticeable difference.

3.2.2 *Flux tube parameters*

The flux tube is the most important part of this model. It defines the volume within the magnetosphere filled with energetic particles and dense, hot thermal plasma, generated by magnetic reconnection at the flux tube apex. The parameters chosen to describe this single event in the flux tube lead to the generation of radio and X-ray emission which are then compared to the scaling relations of Section 2. Therefore, to gain reasonable and comparable , many parameter values need to be carefully chosen. These parameters include: thermal density, non-thermal density, temperature, electron pitch angle. and electron energy distribution. As we are interested in the variable radio emission, the non-thermal density is the most important of these values. The non-thermal population gives a dominant contribution to the gyrosynchrotron radiation.

The 'standard' flux tube temperature used in the model is 30 MK. There are many reports of large YSO flares exceeding 100 MK including those observed by Grosso et al. (2004) and Franciosini et al. (2006). However, the majority of the literature detailing T-Tauri flares suggests an average of around 30 MK. Where data from two-temperature fits of X-ray data is available, the second, highest temperature is examined and agrees with our 'standard' assumption of 30 MK.

The electron pitch angle distribution is kept at the default setting of isotropic. The electron energy distribution is also kept at the default: a single power law. A power law is commonly used for non-thermal astrophysical plasmas. This power law is given as,

$$n(\epsilon)d\epsilon = A\epsilon^{-\delta}d\epsilon \tag{11}$$

for $\epsilon_0 < \epsilon < \epsilon_{\mathrm{max}}$ where A is a normalization constant. The energy range is defined in the GX simulator as $10\mathrm{keV} < \epsilon < 100$ MeV. There is insufficient information about the flares of interest to consider any more complicated distributions. For gyrosynchrotron emission from a power-law distribution the accepted range of δ (the power-law index) values is $2 < \delta < 7$. A value of 3.2 is chosen for this model (as suggested by the GX simulator); however, the effect of a larger delta is explored in Section 4. A value of 3 or lower is often applied to solar flares (Benz 2008 and Fletcher et al. 2011).

It is more difficult to determine an accurate value for the thermal and non-thermal densities in the flux tube. Some assumptions are made along with literature results to determine an initial 'standard' value. The first of these assumptions is that the densities are generally larger than those reported from solar flares (10^8–10^{11} cm^{-3}) (Benz 2008). Stellar flare densities are often reported in literature in the range 10^9–$10^{12.75}$ cm^{-3} both through observations (Favata et al. 2005; Smith et al. 2005; Giardino et al. 2006a; Getman et al. 2008) and modelling (Isobe et al. 2003; Reale et al. 2018). The second is that the non-thermal density should always be lower than the thermal density. When a solar flare occurs, the coinciding emission of soft X-ray and microwave emission is observable. This effect is known as the Neupert effect. The idea of a link between particle acceleration (microwave) and plasma heating (X-rays) has been discussed above. However, when there is no flaring activity, there still remains a level of background thermal radiation. Indeed, a simulation is performed with zero non-thermal particles to model gyrosynchrotron radiation (see Fig. 12 in Section 4) from thermal plasma.

Based on background coronal density values from the literature, it is suggested that 5×10^{11} cm^{-3} is a suitable value for the thermal number density with the 'standard' non-thermal density being set as half that (Güdel et al. 2001; Imanishi et al. 2003; Huenemoerder et al. 2007). The range of non-thermal densities trialled later on range from zero to the normal thermal density (5×10^{11} cm^{-3}).

The flux tube cross-section defines the set of magnetic field lines which is filled with heated plasma and energetic particles, as shown in Fig. 2, which is determined by the scale of the interaction region between the magnetosphere and the disc, where reconnection occurs. This cannot be determined directly through observations at present, but based on the observed aspect ratio of solar flare loops and on numerical models, a width to length ratio of 0.1 seems plausible (Kawamichi 2007). As discussed above, the loop is chosen to extend to $4\,\mathrm{R}_\odot$ (where it interacts with the disc) and the loop lengths are of the order of $10\,\mathrm{R}_\odot$; therefore, we take the standard loop diameter to be $1\,\mathrm{R}_\odot$, whilst later considering this parameter to vary over the range $0.5\,\mathrm{R}_\odot$–$2\,\mathrm{R}_\odot$. Evidently, the choice of width affects the volume of the emitting region (proportional to the square of the width) and hence both the emission measure and the luminosities (in X-ray and radio). Our chosen standard flux tube width is consistent with the observed magnitudes of these quantities.

3.2.3 *Coronal parameters*

The two coronal parameters to be altered are the coronal temperature and coronal density. Both these quantities are set at the base of the cube and decrease with increasing radii. It is assumed that in the T-Tauri's magnetosphere both the coronal density and temperature are lower than the corresponding flux tube quantities. There is no flux tube near the surface (in this model), so the (background) coronal density is purely thermal.

The coronal temperature, or the quiescent low temperature of the non-flaring material, is described as having a range of values by Güdel et al. (2001) and Telleschi et al. (2007). The lowest values tend to be around 1 MK with the highest of the most active TTSs being around 50 MK. The majority of the literature suggests coronal temperatures of TTSs to be around 7 MK, so this is chosen as the normal value (Franciosini et al. 2006; Dahm et al. 2007; Johnstone et al. 2013). This is also in agreement with the lower value from 2-temperature fits of X-ray data.

The standard value for the coronal density was chosen to be $10^{10}\,\mathrm{cm}^{-3}$ (Güdel et al. 2001). This value is appropriate considering the other chosen 'standard' parameters and values for a typical T-Tauri magnetosphere (Güdel et al. 2001; Iman-

Table 2. Parameters that are varied within the GX simulator model to represent a T-Tauri star. Their standard value is shown along with the range within which they are varied. B, n_c, n_0, T_c, T, n_b, δ, w correspond to the surface magnetic field strength, coronal density, non-thermal flux tube density, coronal temperature, flux tube temperature, non-thermal flux tube density, power law index and flux tube width respectively. A dash in the final column indicates the parameter was not varied. Results of these simulations are discussed in Section 4.

Parameter	Standard value	Model range
B / kG	2	1 – 6
n_c / cm^{-3}	10^{10}	–
T_c / MK	7	–s
n_0 / cm^{-3}	5×10^{11}	$2.5 \times 10^{11} – 1 \times 10^{12}$
T / MK	30	10-90
n_b / cm^{-3}	2.5×10^{11}	$0 – 5 \times 10^{11}$
δ	3.2	2–7
w / $R_\odot$	1	0.5–2

ishi et al. 2003; Huenemoerder et al. 2007; Hartmann et al. 2016).

As we are primarily concerned with a flaring scenario, the coronal parameters are not altered and remain at these values throughout all our simulations. This is reflected in Table 2 which displays all the altered parameters in the GX simulator, their standard value, and the range of values also modelled.

4 RESULTS

4.1 Standard model

Fig. 7 shows typical total intensity (right plus left hand circular polarization) emission maps that result from the rendering of the data cube containing the flux tube at 5, 10, and 20 GHz. The parameters used in this simulation are those listed as 'standard' in Table 2. This model and its spectra will henceforth be referred to as the standard model which all other models are compared against. The three colour bars in Fig. 7 are specific to each image and are measured in solar flux units (where 1 sfu $= 10^4$ Jy) at an assumed distance of 1 AU. Fig. 8 shows the corresponding spectra from this simulation between frequencies of 1 and 100 GHz. The emission becomes optically thin and turns over at frequencies higher than around 20 GHz.

While the previous figures show the results for radio rendering, the GX simulator also generates X-ray results. With both the radio and X-ray data from this model, the corresponding luminosities can be calculated and plotted allowing for comparison with Fig. 3. This is displayed in Fig. 4 as shown earlier. The original observational data from Fig. 3 is shown close up along with the result of the standard model (the black dot). Clearly, the standard model generates radio and X-ray luminosities that both agree with the observational results but also lie below the Güdel–Benz relation.

Varying this standard model garners more information on what effect different parameter changes has on the result from Fig. 4 and is discussed next. By varying the parameters in Table 2, we can generate a grid of model points that represent the theoretical limits to a stellar flare. We can also examine the results of the different spectra produced in these different simulations. The restriction of only changing one or two parameters at a time is made; future simulations could vary all parameters appropriately, e.g. to model a large flare where every value is maximized.

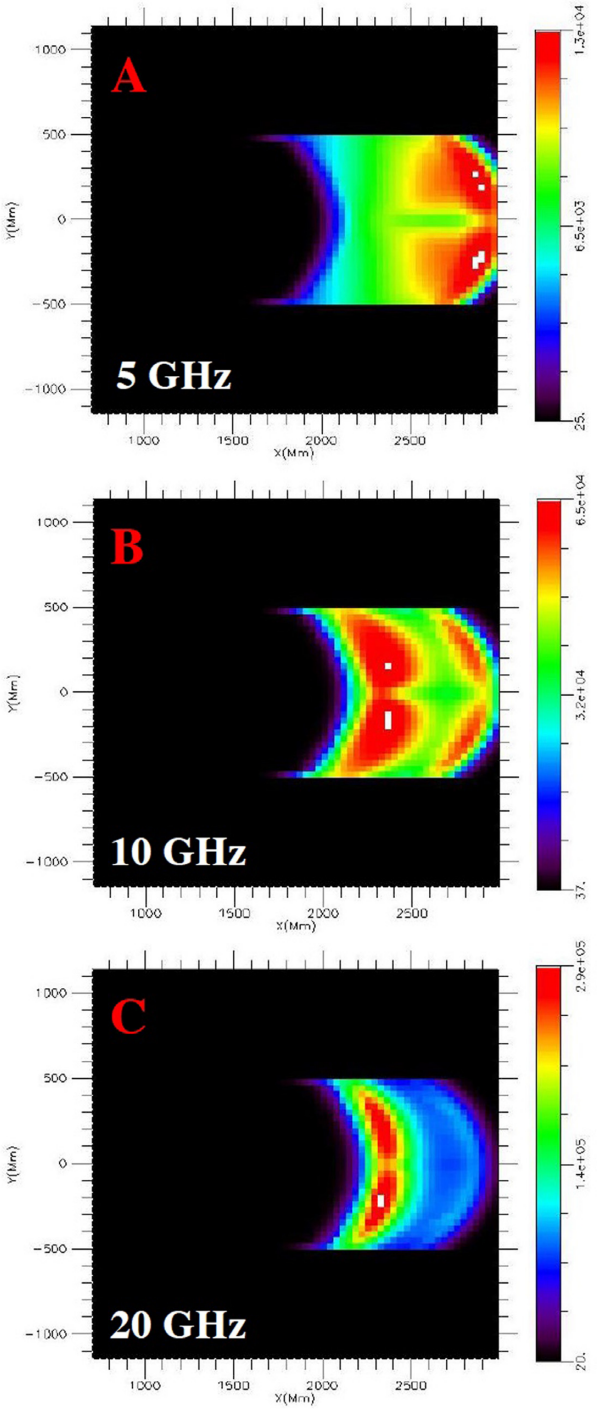

Figure 7. Radio emission maps produced from the rendering of the GX simulator model with parameters described in the second column of Table 2. Figs A, B, and C show the results at 5, 10, and 20 GHz, respectively. Colour bars beside each image are specific to them, with fluxes measured in solar flux units (where 1 sfu $= 10^4$ Jy). The distance from which these fluxes are measured is set at 1 AU.

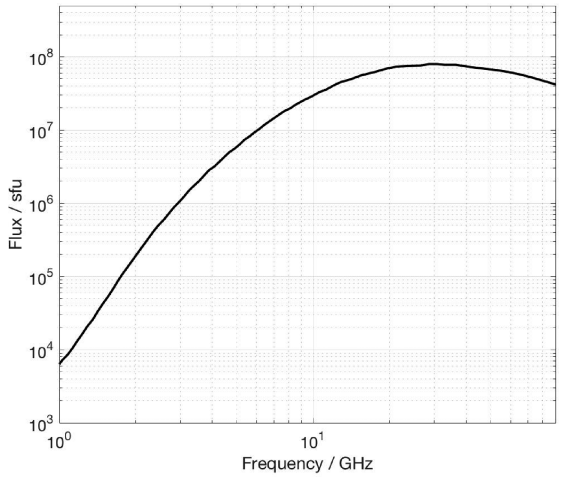

Figure 8. Simulated radio spectrum with standard parameters. The GX simulator cuts off past 100 GHz but the optically thin limit is reached past around 20 GHz. The peak flux is approximately 10^8 sfu with a corresponding frequency of around 30 GHz.

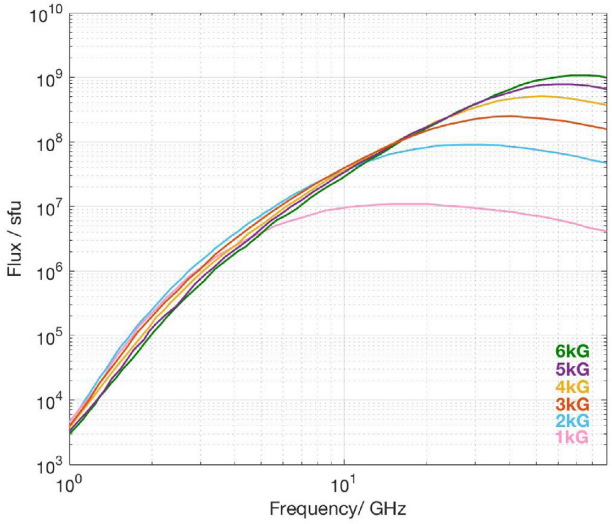

Figure 9. Radio spectra from six different magnetic field strength simulations: 1, 2, 3, 4, 5, and 6 kG (pink, blue, orange, yellow, purple, green). The standard result of Fig. 8 is shown as the blue, 2 kG line. The highest field strengths give the largest peak fluxes and corresponding frequencies. The flux is given in solar flux units.

4.2 Varying the standard parameters

4.2.1 Magnetic field

The effect of varying the surface magnetic field strength between 1 and 6 kG is shown in Fig. 9. The main range later used in varying the field strength with other parameters is 1–4 kG. The results from a purely dipolar model are nearly identical to the primary multipolar model except at smaller distances to the stellar surface where the emission from a purely octupolar field becomes significant. This is because the octupolar field strength falls off with distance as r^{-9} compared with r^{-3} for the dipolar field. The shape of the spectra for an increasing field remains similar to that of Fig. 8 (blue line in Fig. 9) but the peak radio flux and frequency increase as the slope's peak shifts slightly to the right. For a surface field strength of 1000 G (and all other model parameters kept as 'standard') the

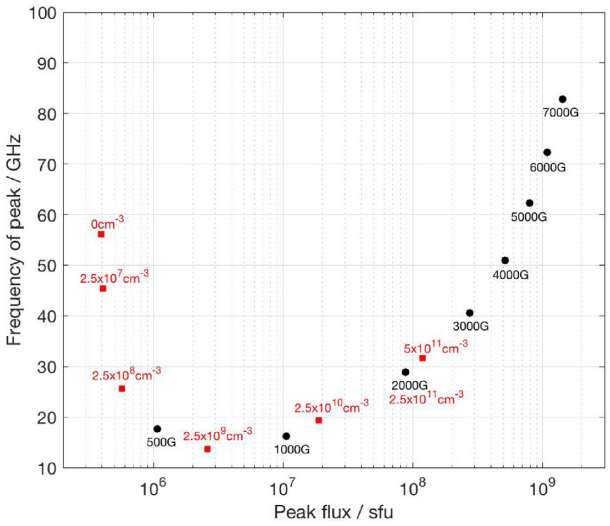

Figure 10. Peak fluxes (where 1 sfu $= 10^4$ Jy) and corresponding frequencies from the spectra of different magnetic field strengths and non-thermal densities. The black points represent a change in magnetic field strength (going one step below and above the standard range in Table 2 to 500 and 7000G). The red points indicate a change in only the non-thermal density. The black point labelled with 2000G and 2.5×10^{11} cm^{-3} is the standard model result from Fig. 4.

peak radio flux and frequency are 1.01×10^7 sfu and 16.26 GHz, respectively. As the field strength increases to 4000 G, these results also increase to 5.01×10^8 sfu and 51.32 GHz.

The spectra in Fig. 9 demonstrate, as expected, that more emission is generated for stronger fields. This nicely supports the link between the much higher luminosity flares observed on T-Tauris than the Sun and also the fact T-Tauris are known to possess larger field strengths and more active magnetospheres.

At low frequencies, the spectra all follow the same general shape and change in flux while the frequency of the peak increases as the field strength increases. The peak fluxes and corresponding frequencies are shown in Fig. 10. The black points represent the peak values from Fig. 9 and show the trend nicely. With every increase of 1 kG of the surface field strength, the factor by which the peak flux changes becomes smaller. Indeed, there is a factor of about 10 difference in the peak fluxes between both 1 kG–2 kG and 2 kG–6 kG. The difference between the frequencies of those peaks is much more uniformly spread, except at the lowest surface field strengths. Hence, locating the spectral peak observationally, potentially gives information about the magnetic field strength. The effect of varying the magnetic field strength on the X-ray and radio luminosities is discussed and shown later in Figs 14, 15, and 17.

4.2.2 Non-thermal density

The non-thermal density is a vital parameter to explore as its effect on the emission maps and spectra can help identify whether reconnection events are occurring. Fig. 11 shows the results of varying this non-thermal population. The absence of non-thermal particles always produces this flat spectra at high frequencies. The lack of these particles also produces a much lower peak in emission compared to when the non-thermal density is, for example, 2.5×10^{10} cm^{-3}. The zero non-thermal density line (purple) in Fig. 11 can be identified especially at these frequencies where there is no distinct peak or

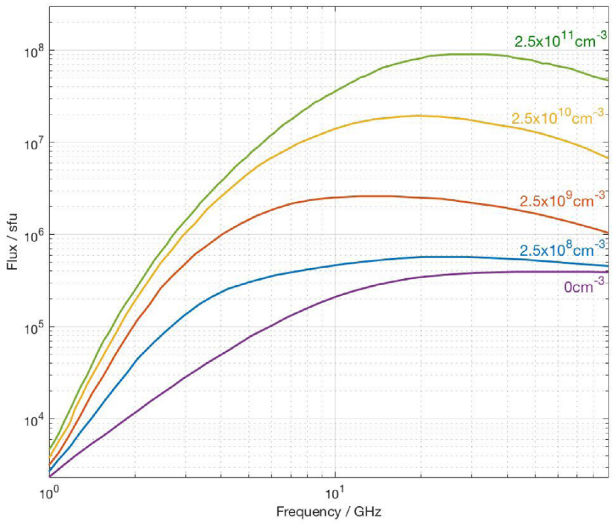

Figure 11. Radio spectra from varying the non-thermal density. The green line is the same as in Fig. 8. Increasing the non-thermal density again to the standard thermal value (5×10^{11} cm^{-3}) resulted in a spectra that followed the pattern shown here. The purple, blue, orange, and yellow lines represent densities of 0, 2.5×10^{8}, 2.5×10^{9}, and 2.5×10^{10} cm^{-3}, respectively. The flux is given in solar flux units.

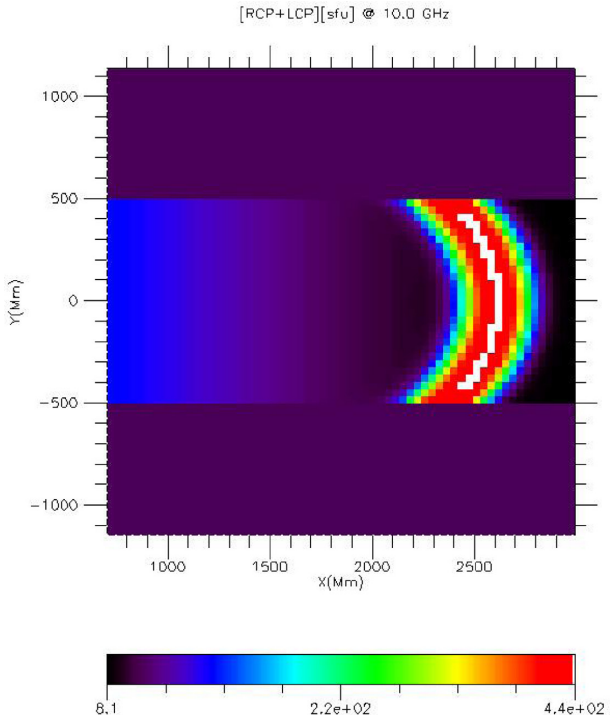

Figure 12. A 10-GHz radio emission map of a model with no non-thermal particles injected (corresponding spectra is the purple line from Fig. 11). The overall flux is a lot lower than when there are non-thermal particles present and as such the background thermal component finally registers. The emission peaks along the central line of the flux tube where the thermal flux tube particles are located.

increase in flux past 10 GHz to indicate the lack of non-thermal particles and no (or at least significant in size) reconnection event.

Considering the emission from the non-thermal particles alone, increasing the density increases the flux and the frequency of peak emission. However, this model includes a contribution to the emission from thermal and non-thermal particle and so the resulting spectrum is a combination of the emission from these. At non-zero thermal density, the spectrum is purely thermal and peaks at high frequency. Introducing a small amount of non-thermal particles produces emission at lower-frequency and this shifts the peak of the combined spectrum to lower frequency. As more non-thermal particles are added, the non-thermal emission becomes stronger and its peak moves to high frequency. The net effect is therefore that initially the non-thermal emission causes the peak to move to a lower frequency (than the purely thermal emission) and then to high frequency as the non-thermal emission dominates and its peak shifts the higher frequency more than the underlying thermal emission. This behaviour can be seen more clearly in Fig. 10.

The emission maps demonstrate this difference also. Fig. 12 shows the results at 10 GHz of the flux tube and inner magnetosphere with no non-thermal particles present. When compared with Fig. 7 it is clear the flux appears much more evenly distributed. As this is purely thermal emission, the peak flux is lower with the background component not being suppressed near the surface. The magnetic field configuration also does not influence the emission from the particles as the thermal population is not driven by the reconnection of field lines. Although it is not possible to observe and resolve individual flares from T-Tauri stars, it is useful to see these emission maps and understand their physical interpretation. It consolidates the fact that non-thermal particles can be observed in flaring-like events which are often seen as varied peaks in spectra or light curves. A further development on this model could involve time dependency and the evolution of the flaring event after reconnection.

As discussed in Section 4.2.1, Fig. 10 shows the peak fluxes and frequencies from the spectra of changing magnetic field models. It also shows the effect of changing the non-thermal density on the peak flux and frequencies from Fig. 11. It is clear that with an increase in non-thermal density the same general trend is followed, i.e. an increase in peak flux. However, the frequency of the peak rises dramatically the closer to zero non-thermal particles the model gets. Also, at lower densities, the peak fluxes are closer together. This is in contrast to the field strengths where at lower values they are further apart.

4.2.3 *Power-law index*

Related to the non-thermal distribution of particles is the power-law index, δ. The standard value of 3.2 is varied to 2, 3, 4, and 7 and the results are shown in Fig. 13.

The lowest delta values produce steep curves which do not peak below 100 GHz. The highest delta values (5 or above) produce this very flat spectra past 10 GHz with a low peak flux around that mark. The optimum value for gaining the peak that does not plateau out is clearly at $\delta = 4$ or smaller. This plot nicely constrains the suitable values for δ for these T-Tauri stars, which had previously been using the value of 3.2 as it is used in solar flares (see Section 3.2.2).

The spectra in Fig. 13 behave in a similar way to that of Fig. 11 and is discussed in Section 4.2.2. A purely thermal spectra has large numbers of low energy particles. When the power-law component is added, it results in more higher energy (non-thermal) particles. For smaller power-law indices, this high energy particle 'tail' increases and there is more gyrosynchrotron emission (and higher peak flux). Similarly to Fig. 11, the high energy (non-thermal) component drags the spectral peak from the low-frequency end to the high-frequency end as the power law index is decreased. However, at high index

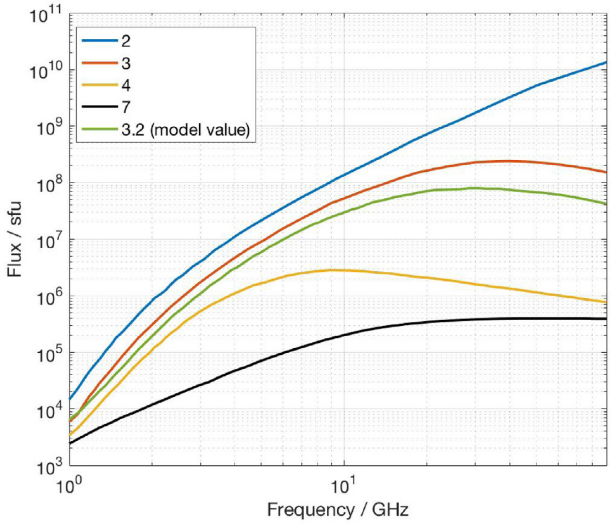

Figure 13. Spectral results of varying the power-law index. The standard model value of 3.2 (green) is varied to 2 (blue), 3 (orange), 4 (yellow), and 7 (black).

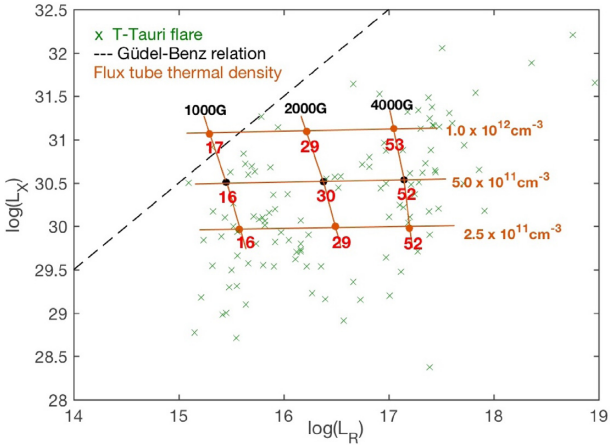

Figure 14. X-ray and radio luminosity plot of observed and modelled flares from a T-Tauri star. Green crosses are as before and all dots are model results. Black points indicate a change in the model's surface field strength between 1, 2, and 4 kG while orange dots indicate the model results of changing the flux tube thermal density between 2.5×10^{11} cm^{-3}, 5×10^{11} cm^{-3}, or 1.0×10^{12} cm^{-3}. The Güdel–Benz relation is shown again. The red numbers indicate the frequencies in GHz of the peak flux for each model.

values (about 7), the spectra appears purely thermal with less non-thermal contribution, so the frequency of the peak is again high (like in Fig. 11). As the high energy component becomes more dominant initially, the combination of these two spectra are seen as the yellow line in Fig. 13, i.e. a spectra with a higher peak flux but lower peak frequency than the thermal (index of 7) spectra.

4.2.4 Flux tube densities and temperature

Two remaining parameters to be varied are the flux tube temperature and flux tube thermal density. The result of varying the flux tube thermal density together with the field strength are shown in Fig. 14. This time, the effects of varying the parameters are shown on the plot which relates X-ray and radio luminosity. Eight additional simulations are performed in addition to the standard model in

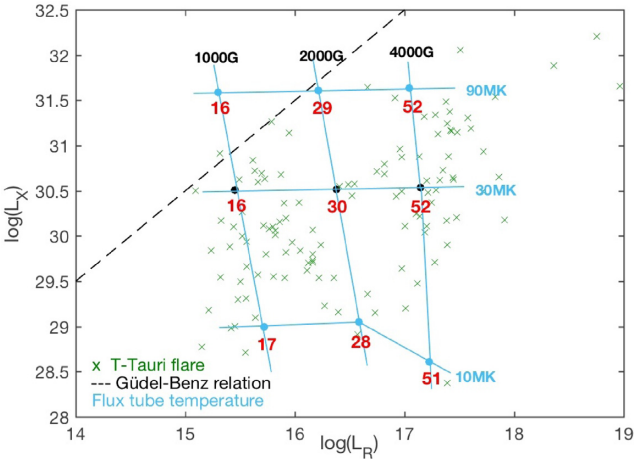

Figure 15. X-ray and radio luminosity plot of observed and modelled flares from a T-Tauri star. Green crosses are as before and all dots are model results. Black points show the model results of changing the surface field strength between 1, 2, and 4 kG while blue dots indicate a change in the model's flux tube temperature between 10, 30, and 90 MK. The Güdel–Benz relation is shown as the dashed line. The red numbers indicate the frequencies in GHz of the peak flux for each model.

Fig. 4. These results form a grid with the columns corresponding to a change in surface field strength and rows tracing a change in flux tube thermal density. For example, the bottom leftmost point indicates the result of a model with the lowest field strength of 1000G and lowest thermal density of 2.5×10^{11} cm^{-3}. This density value is chosen so as the thermal density is never lower than the non-thermal density. The grid allows for the constraint of the physical parameters of a flare.

Looking at the change in field strength across Fig. 14, it is clear that the radio luminosity increases dramatically over a 3000G increase in field strength when compared with the X-ray. The X-ray luminosity plotted here is thermal (soft) and so it is not expected to change in a similar manner as the non-thermal radio. An increase in field strength also appears to lead to a smaller increase in radio luminosity at larger and larger fields (not shown, although peak fluxes of higher field models are shown in Fig. 10). The change in field strength also has an effect on the frequencies of the peaks. The lowest field strengths have lower peak frequencies for a range of density values when compared with higher field strengths for the same density range.

The higher the thermal density, the larger the X-ray luminosity is. This is to be expected as an increase in thermal particles will lead to an increase in thermal emission, i.e. soft X-rays. There is a very slight decrease in the radio luminosity with large thermal densities, due to optical depth effects.

Overall, these nine models agree well with the observational results. They all lie in a similar luminosity range for both X-ray and radio. The models nearly all lie below the Güdel–Benz relation, with only the lowest field strength model with the highest density being slightly above the line. This model describes a star where less non-thermal emission (and therefore less radio emission) is produced but there are high levels of thermal emission. An increase in thermal emission without a corresponding increase in non-thermal emission is not indicative of a flaring event.

A similar plot is shown in Fig. 15. This plot shows the results of simultaneously varying the surface field strength and flux tube temperature. This is expected to have a large effect on the thermal

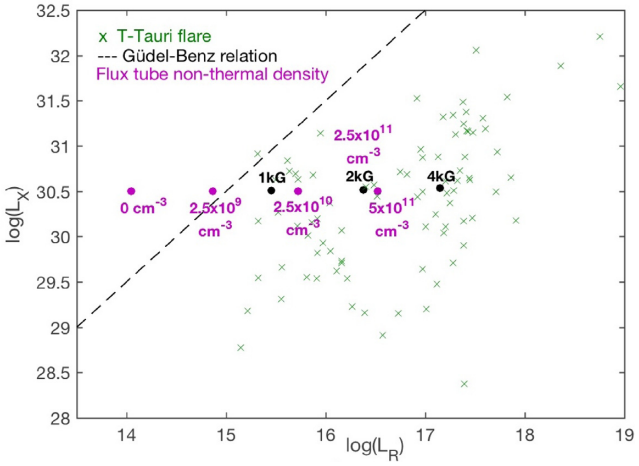

Figure 16. X-ray and radio luminosity plot of observed and modelled flares from a T-Tauri star. Green crosses are as before and all dots are model results. Black points indicate a change in surface field strength ranging from 1, 2, and 4 kG while purple dots indicate a non-thermal flux tube density of 0 cm^{-3}, 2.5 × 10^9 cm^{-3}, 2.5 × 10^{10} cm^{-3}, 2.5 × 10^{11} cm^{-3} (black dot), and 5 × 10^{11} cm^{-3}. The Güdel–Benz relation is shown as the dashed line.

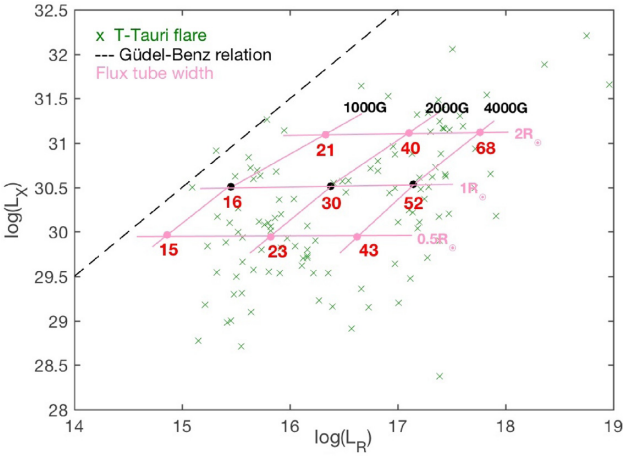

Figure 17. X-ray and radio luminosity plot of observed and modelled flares from a T-Tauri star. Green crosses are as before and all dots are model results. Black points indicate models of varying surface field strength ranging from 1, 2, and 4 kG while pink dots indicate models with varying flux tube widths of 0.5, 1, and 2$_\odot$. The Güdel–Benz relation is shown as the dashed line. The red numbers indicate the frequencies in GHz of the peak flux for each model.

emission like the flux tube thermal density did. This is clearly seen in the results in Fig. 15 with a large increase in X-ray luminosity for increasing flux tube temperature. Again, there is the small fluctuation in radio luminosity. The three temperatures used in these nine simulations are 10, 30, and 90 MK. The spread in the grid is much larger than in Fig. 14 but still fits with the observational results. While the X-ray luminosity increases for higher temperatures when combined with an increasing field, the model has both high X-ray and radio luminosities.

The frequencies of the peak fluxes from these models are shown again to follow the magnetic field strengths. Even for a large difference in X-ray luminosity between 10 and 90 MK, the frequency peaks at around 16 GHz for a surface field strength of 1 kG. The three field values (1, 2, 4 kG) and their associated frequencies (approximately 16, 29, and 52 GHz) are the same here as for the previous thermal density plot.

An increase in temperature in a flaring event is associated with the sudden plasma heating caused by magnetic reconnection. This is accompanied by particle acceleration leading to the increase of non-thermal emission. The effect of varying the non-thermal density on this radio and X-ray luminosity plot is shown in Fig. 16. There is a degeneracy between the results of increasing the non-thermal emission and field strength. Increasing the non-thermal density from the central black point leads to results which move across the plot along the same line as the increasing field strengths do (as expected from Fig. 11 as the flux increases with increasing density), i.e. towards higher radio luminosities.

4.2.5 Flux tube width

One final parameter that has so far remained unchanged is the width of the flux tube. It has been maintained at a diameter of 1 $R_\odot$ in the previous models but it will now be varied between 0.5 $R_\odot$ and 2 $R_\odot$. While the thermal density and flux tube temperature varied so far have primarily affected the thermal emission, the width of the flux tube will likely affect both the X-ray and radio luminosities.

Changing the width of the loop, at fixed density, evidently affects the emission measure as shown in equation (3), and thus for a given density, there are clearly limits on the range of loop widths which are expected. Nevertheless, it is useful to explore the effect of varying the value of the flux rope width, especially as this is a parameter whose value cannot easily be measured (see Section 3.2.2). Broadly speaking, making the flux tube bigger increases the volume of the emitting region and thus will increase the luminosities and the emission measure, but this is complicated by the non-uniformity of the system and optically-thick effects, and so is worth investigating.

The results of trialling this in the GX simulator is shown in Fig. 17. In contrast to the previous two plots, the varying of flux tube width produces results which move parallel to the Güdel–Benz relation and the observed sources themselves. As expected, there is a similar change in both X-ray and radio luminosity along the grid lines of constant field.

A smaller region does not indicate more of an agreement with the Güdel–Benz relation. It only leads to lower luminosities. So, although the smaller flaring regions associated with solar flares may agree with the relation, Fig. 17 suggests that it is not the size of the region alone that leads to this agreement.

The frequencies corresponding to the peak fluxes for each model are similar to what has previously been seen for flux tube temperature and thermal density. The frequency follows the lines of magnetic field strength, generally increasing for a larger field. However, here the lines of constant field strength are more slanted, giving peak frequencies that vary more that before for a single field value when the flux tube width is changed.

5 SUMMARY AND CONCLUSIONS

The radio and X-ray emission in flare-like events from T-Tauri stars has been shown to be far more luminous than that of solar and other main sequence stellar flares. From an analysis of a large data set of observations reported in the literature, we have shown that the T-Tauri stars show consistent and significant deviations from the Güdel–Benz scaling relation, which describes the X-ray – radio correlation for solar and main-sequence stellar flares. These young active stars show significantly higher than expected levels of radio luminosities relative to their X-ray luminosities.

In order to explore a physical explanation of these observations, we have developed for the first time a model of the emission from flares in young stars, building on understanding of solar flare processes whilst using the best available knowledge of the relevant physical parameters of T-Tauri stars. We consider the flare result from of a large magnetic flux tube within the stellar magnetosphere, with enhancements of temperature and density relative to the ambient atmosphere. This flux tube is filled with a non-thermal population of energetic electrons which arise from magnetic reconnection activity involving the accretion disc (or a remnant thereof). We do not model the energy release process itself, treating it only as a source of high-energy particles and plasma heating and then use the powerful GX simulator tool to predict the resultant radio and X-ray emission. Despite the simplicity of the model, the predicted X-ray and radio luminosity agree very well with the observations. In particular, the modelled results show a departure from the Güdel–Benz relation similar to the observations, and the predicted distribution of data points in the radio/X-ray luminosity plane is very similar to the observed spread.

We have investigated the effects of varying parameters such as surface magnetic field strength, the dimensions of the flaring flux tube, thermal plasma temperature, and density, and the number density of non-thermal particles. The range of observations are consistent with magnetic field strengths in the range of 1 kG–4 kG and flux tube widths between $0.5\,R_\odot$ and $2.0\,R_\odot$ with gas temperatures in the range between 10 MK and 90 MK. The models indicate the radio emission peaks at frequencies >10 GHz and in some cases beyond the upper frequency limit of our modelling, 100 GHz. These frequencies are significantly higher than have been previously used to study the radio variability of young stars.

There is naturally some (near) degeneracy of the model parameters in terms of the predicted luminosities, for example, between magnetic field strength and non-thermal density. However, the models provide a useful guide to interpretation of future observations, in particular showing how the frequency of peak emission, and the flux at this peak, depend on magnetic field and non-thermal particles.

From the model results it is clear that the factors that definitely affect the proximity to the standard Güdel–Benz relation are an increase in the thermal dependent components (flux tube temperature and thermal density) and a decrease in the non-thermal dependent components (non-thermal density and field strength). As it is known that the field strengths of these stars are large, it is reasonable to assume it is the field and therefore non-thermal emission generating reconnection events that lead to the deviation from the relation.

Our model can produce objects with emission close or on to the Güdel–Benz, but an increase in temperature or thermal density to do this would require values of these quantities that have been rarely or never reported and so seem unrealistic. Similarly, the increased size of the emission region in our model, the flux tube, cannot alone account for the increased radio emission of the young sources compared with that predicted by the Güdel–Benz relation. Nevertheless, one important point is that in these large flux tubes the accelerated particles are likely to be magnetically trapped for far longer than solar flare particles and continue radiating as they are bounced between the footpoints. Exploring the observable impact of this requires future, time-dependent models.

Weak-lined T-Tauri stars (class III objects) have little or no active accretion but still show quite similar radio and X-ray behaviour as the classical T-Tauri stars (class II objects) (Fig. 4). Our analysis shows that there is no difference in the X-ray properties between the two classes of objects, but perhaps a marginal difference in their radio properties. These observations and our models suggest that the weak-lined stars may have quite similar magnetic interactions to classical T-Tauri stars, despite the lack of an observable disc. However, a detailed comparison and analysis of any evolutionary trends requires focused, population studies.

Differences between T-Tauri events and those in main sequence and solar flares may also result from how the energy release is triggered. In the latter case, free magnetic energy is built up in the magnetic field, with magnetic reconnection triggered through onset of an instability or loss of equilibrium in the coronal field; in the former, the reconnection occurs at much higher altitudes due to interactions between the magnetosphere and the disc magnetic field. Both the geometry of the magnetic reconnection, and the physical environment (e.g. the presence of dense weakly ionized plasma in the disc) differ substantially between the two scenarios, and this may affect the dynamics and the energy-partition. These differences will be considered in future models to get a more complete understanding of these systems.

More comprehensive observations, including simultaneous X-ray and multi-frequency radio observations, are needed of large samples of T-Tauri stars to better constrain the nature and variability of their radio emission and the physical properties of the emitting regions. Such radio surveys with high time cadence have been proposed for SKA (Fuller et al. 2015). Similarly, missions such as Athena (Barcons et al. 2017) will provide opportunities for X-ray observations of flares on YSOs. Our models provide a useful guide to interpretation of such observations. Future modelling will investigate more detailed and realistic models of the stellar magnetospheres, and investigate the dynamics of the magnetic reconnection arising through interactions with the disc.

ACKNOWLEDGEMENTS

COGW is grateful to STFC (Science and Technology Facilities Council) for studentship support under grant ST/N504178/1. PKB and MG acknowledge STFC support through the consolidated grant ST/P000428/1.

REFERENCES

Alencar S. H. P. et al., 2012, A&A, 541, A116
Argiroffi C., Favata F., Flaccomio E., Maggio A., Micela G., Peres G., Sciortino S., 2006, A&A, 459, 199
Barcons X. et al., 2017, Astron. Nachr., 338, 153
Benz A. O., Güdel M., 1994, A&A, 285, 621
Benz A. O., 2008, Living Rev. Solar Phys., 5, 1
Benz A. O., Güdel M., 2010, ARA&A, 48, 241
Dahm S. E., Simon T., Proszkow E. M., Patten B. M., 2007, AJ, 134, 999
Donati J.-F. et al., 2010, MNRAS, 409, 1347
Donati J.-F. et al., 2012, MNRAS, 425, 2948
Dzib S. A. et al., 2013, ApJ, 775, 63
Dzib S. A. et al., 2015, ApJ, 801, 91
Favata F., Flaccomio E., Reale F., Micela G., Sciortino S., Shang H., Stassun K. G., Feigelson E. D., 2005, ApJ Suppl. Ser., 160, 469
Feigelson E. D., Montmerle T., 1999, ARA&A, 37, 363
Feldman U., Laming J. M., Doschek G. A., 1995, ApJ, 451, L79
Fleishman G. D., Kuznetsov A. A., 2010, ApJ, 721, 1127
Fletcher L. et al., 2011, Space Sci. Rev., 159, 19
Forbrich J., Osten R. A., Wolk S. J., 2011, ApJ, 736, 25
Franciosini E. et al., 2006, A&A, 468, 485
Fuller G., Forbrich J., Rathborne J., Longmore S., Molinari S., 2015, Proc. Sci., Star and Stellar Cluster Formation: ALMA-SKA Synergies. SISSA, Trieste, PoS(AASKA14)152
Gagné M., Skinner S. L., Daniel K. J., 2004, ApJ, 613, 393
Getman K. V. et al., 2005, ApJ Suppl. Ser., 160, 319

Getman K. V., Feigelson E. D., Micela G., Jardine M. M., Gregory S. G., Garmire G. P., 2008, ApJ, 688, 437
Getman K. V., Broos P. S., Salter D. M., Garmire G. P., Hogerheijde M. R., 2011, ApJ, 730, 6
Giardino G., Favata F., Silva B., Micela G., Reale F., Sciortino S., 2006a, A&A, 453, 241
Giardino G., Favata F., Micela G., Sciortino S., Winston E., 2006b, A&A, 463, 275
Giardino G., Favata F., Micela G., S. Sciortino Winston E., 2007, A&A, 464, 275
Gregory S., Donati J.-F., 2011, Astron. Nachr., 332, 1027
Gregory S. G., Matt S. P., Donati J.-F., Jardine M., 2008, MNRAS, 389, 1839
Gregory S. G., Jardine M., Gray C. G., Donati J.-F., 2010, Rep. Progr. Phys., 73, 126901
Grosso N., Montmerle T., Feigelson E. D., Forbes T. G., 2004, A&A, 419, 653
Grosso N., Bouvier J., Montmerle T., Fernández M., Grankin K., Osorio M. R. Z., 2007, A&A, 475, 607
Güdel M., 1992, A&A, 264, L31
Güdel M., Benz A. O., 1993, ApJ, 405, L63
Güdel M., Schmitt J. H. M. M., Bookbinder J. A., Fleming T. A., 1993, ApJ, 415, 236
Güdel M. et al., 2001, A&A, 365, L336
Güdel M. et al., 2006, A&A, 468, 353
Hartmann L., Herczeg G., Calvet N., 2016, ARA&A, 54, 135
Huenemoerder D. P., Kastner J. H., Testa P., Schulz N. S., Weintraub D. A., 2007, ApJ, 671, 592
Hussain G. A. J. et al., 2009, MNRAS, 398, 189
Imanishi K., Koyama K., Tsuboi Y., 2002, ApJ, 579, 920
Imanishi K., Nakajima H., Tsujimoto M., Koyama K., Tsuboi Y., 2003, Publ. Astron. Soc. Jpn., 55, 653
Isobe H., Shibata K., Yokoyama T., Imanishi K., 2003, Publ. Astron. Soc. Jpn., 55, 967
Johns-Krull C. M., 2007, ApJ, 664, 975
Johns-Krull C. M. et al., 2013, ApJ, 765, 11
Johnstone C. P., Jardine M., Gregory S. G., Donati J.-F., Hussain G., 2013, MNRAS, 437, 3202
Kawamichi T. . S. K., 2007, New Solar Phys. Solar-B Mission, 369, 505
Kounkel M. et al., 2014, ApJ, 790, 49
Kuhn M. A., Getman K. V., Feigelson E. D., Reipurth B., Rodney S. A., Garmire G. P., 2010, ApJ, 725, 2485
Long M., Romanova M. M., Lamb F. K., 2012, New Astron., 17, 232
López-Santiago J., Crespo-Chacón I., Flaccomio E., Sciortino S., Micela G., Reale F., 2016, A&A, 590, A7
McKee C. F., Ostriker E. C., 2007, ARA&A, 45, 565
Nita G. M., Fleishman G. D., Kuznetsov A. A., Kontar E. P., Gary D. E., 2015, ApJ, 799, 236
Orlando S., Reale F., Peres G., Mignone A., 2011, MNRAS, 415, 3380
Ortiz-León G. N. et al., 2015, ApJ, 805, 9
Osten R. A., Wolk S. J., 2009, ApJ, 691, 1128
Pillitteri I. et al., 2010, Astron. Astrophys., 519, A34
Ramírez S. V. et al., 2004, AJ, 128, 787
Reale F., Lopez-Santiago J., Flaccomio E., Petralia A., Sciortino S., 2018, ApJ, 856, 51
Schulz N. S., Huenemoerder D. P., Günther M., Testa P., Canizares C. R., 2015, ApJ, 810, 55
Shibata K., Yokoyama T., 1999, ApJ, 526, L49
Skinner S., Gagne M., Belzer E., 2003, ApJ, 598, 375
Smith K., Audard M., Güdel M., Skinner S., Pallavicini R., 2005, in Favata F., Hussain G. A. J., Battrick B., eds, Proc. of 13th Cambridge Workshop on Cool Stars, Stellar Systems and the Sun. ESA SP-560, European Space Agency, Hamburg, Germany, p. 971
Stauffer J. et al., 2014, AJ, 147, 83
Telleschi A., Güdel M., Briggs K. R., Audard M., Palla F., 2007, A&A, 468, 425
Tsuboi Y., Koyama K., Murakami H., Hayashi M., Skinner S., Ueno S., 1998, ApJ, 503, 894
Tsuboi Y. et al., 2016, Publ. Astron. Soc. Jpn., 68, 90
Tsujimoto M., Koyama K., Tsuboi Y., Goto M., Kobayashi N., 2002, ApJ, 566, 974
Umemoto T., Saito M., Nakanishi K., Kuno N., Tsuboi M., 2009, 402, 400
Uzawa A. et al., 2011, Publ. Astron. Soc. Jpn., 63, S713
Warmuth A., Mann G., 2013, A&A, 552, A86

This paper has been typeset from a TEX/LATEX file prepared by the author.